ARTICLE

Neutral Metal-Chelating Compounds with High ^{64}Cu Affinity for PET Imaging Applications in Alzheimer's Disease

Received 00th January 20xx,
Accepted 00th January 20xx

DOI: 10.1039/x0xx00000x

Yiran Huang,[a] Truc T. Huynh,[b,c] Liang Sun,[a] Chi-Herng Hu,[a] Yung-Ching Wang,[a] Buck E. Rogers,[b,*] and Liviu M. Mirica[a,d,*]

Positron emission tomography (PET), which uses positron-emitting radionuclides to visualize and measure processes in the human body, is a useful noninvasive diagnostic tool for Alzheimer's disease (AD). The development of longer-lived radiolabeled compounds is essential for further expanding the use of PET imaging in healthcare, and diagnostic agents employing longer-lived radionuclides such as ^{64}Cu ($t_{1/2}$ = 12.7 h, β^+ = 17%, β^- = 39%, EC = 43%, E_{max} = 0.656 MeV) are capable of accomplishing this. One limitation of ^{64}Cu PET agents is that they could release free radioactive Cu ions from the metal complexes, which decreases the signal to noise ratio and accuracy of imaging. Herein, a series of 1,4,7-triazacyclononane (TACN) and 2,11-diaza[3.3]-(2,6)pyridinophane (N4)-based metal-chelating compounds with pyridine arms were designed and synthesized by incorporating Aβ-interacting fragments into metal-binding ligands, which allows for excellent Cu chelation without diminishing their Aβ-binding affinity. The crystal structures of the corresponding Cu complexes confirmed the pyridine N atoms are involved in binding to Cu. Radiolabeling and autoradiopraphy studies show that the compounds efficiently chelate ^{64}Cu, and the resulting complexes exhibit specific binding to the amyloid plaques in the AD mouse brain sections vs. WT controls.

Introduction

Alzheimer's disease (AD) is the most common neurodegenerative disease. For example, in the United States more than 5 million Americans are living with AD, and this number is expected to reach 16 million by 2050.[1] Positron emission tomography (PET) is a functional imaging technique which can be used for the diagnosis of AD.[2, 3] To date, ^{11}C- and ^{18}F-radiolabeled imaging agents have been tested for PET studies in AD patients, such as Pittsburgh compound B, Florbetapir, and Florbetaben.[2, 4-10] However, the use of these agents is limited due to their short physical half-lives ($t_{1/2}$ = 20.4 min and 109.8 min for ^{11}C and ^{18}F, respectively) and complicated syntheses.

Therefore, the development of radioimaging agents containing longer-lived radionuclides is important, as it would lead to a longer-time diagnostic imaging agent with a better contrast. ^{64}Cu ($t_{1/2}$ = 12.7 h) has become a useful radionuclide in the development of radiopharmaceuticals for imaging purposes.[11-19] The half-life of ^{64}Cu is excellent because it is long enough to allow for imaging at late time points, but not so long that it takes weeks to completely decay. In addition, such a half-life will also allow for the imaging agents to be shipped and used in remote areas. Moreover, the radiolabeling with ^{64}Cu is always the last step in the synthesis of the ^{64}Cu PET imaging agents, thus simplifying their development.[20]

One key limitation of ^{64}Cu PET imaging agents is that they could release ^{64}Cu ions in the human body, especially if some ligands have moderate Cu affinity. Also, some enzymes can reduce the chelated Cu^{2+} into Cu^{+}, which leads to further releasing of ^{64}Cu ions. Consequently, decreasing the free ^{64}Cu level requires ligands to have significantly high metal-binding affinity, limited ligand exchange kinetics, and also relatively low $Cu^{II/I}$ reduction potentials. In our previous report, a series of ^{64}Cu-PET imaging multifunctional compounds (MFCs) were obtained by linking macrocyclic chelators and Aβ-interacting fragments together.[21-25] To further increase the metal-binding affinity, larger multidentate ligands were taken into consideration, such as cross-bridged 1,4,7,10-tetraazacyclododecane (Cyclen) and 1,4,8,11-tetraazacyclotetradecane (Cyclam).[26-29] However, these ligands are too large and they tend to reduce the Aβ-binding affinity of the corresponding multifunctional compounds.

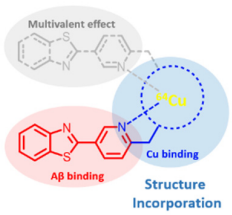

[a] Department of Chemistry, University of Illinois at Urbana-Champaign, 600 S. Mathews Avenue, Urbana, Illinois 61801, United States
[b] Department of Radiation Oncology, Washington University School of Medicine, St. Louis, Missouri 63108, United States
[c] Department of Chemistry, Washington University, St. Louis, MO 63130, United States
[d] Hope Center for Neurological Disorders, Washington University School of Medicine, St. Louis, MO 63110, United States

Electronic supplementary information (ESI) available: Experimental section and Fig. S1–S8. See DOI: 10.1039/x0xx00000x

Fig. 1 Structure incorporation strategy with the red oval representing the Aβ binding fragment and the blue circle representing the metal chelation moiety.

Herein, we introduce a series of metal-chelating compounds (MCCs) designed by employing the strategy of incorporating the Aβ-binding fragment into the metal-chelating moiety (Fig. 1), and by utilizing simple synthetic steps to generate MCCs with high affinities for both ^{64}Cu- and Aβ species.

Results and discussion

Design and Synthesis of Metal-Chelating Compounds

Metal-chelating compounds (MCCs) were designed through the incorporation strategy by merging chemical structures of Aβ binding moiety with a metal-chelating ligand.[30-33] The synthetic route of MCCs starts with oxidative cyclization of 2-aminothiophenol and 6-methylnicotinaldehyde, followed by N-bromosuccinimide (NBS) bromination for further conjugation with the multidentate ligands (Scheme 1). The MCCs were then chelated with $^{64}CuCl_2$ in 0.1 M NH_4OAc (pH 5.5) and the ^{64}Cu-complexes were used without further purification (radiochemical yield > 95%).

Scheme 1 Synthetic routes and structures of the MCCs. The metal-binding parts and Aβ-interacting fragments are shown in blue and red, respectively.

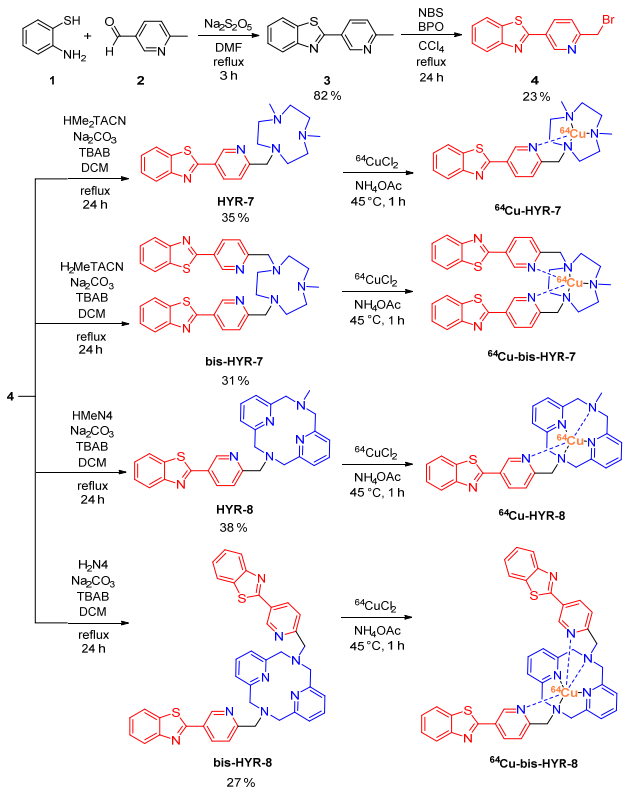

Acidity Constants of the MCCs

Since all the compounds contain several basic functional groups, their acidity constants (pKa) were determined by UV-vis spectrophotometric titrations. For **HYR-7**, titrations from pH 1.0 to 11.0 reveal several changes in the spectra (Fig. 2). The best fit to the data was obtained with four pKa values: 1.06(9), 2.68(7), 5.45(3) and 8.82(2). Based on previously reported acidity constants for amine-pyridine systems,[33-37] we assigned the lowest pKa value to the protonation of the pyridine group, and the other three higher values correspond to macrocyclic amino groups, as is usually observed for TACN derivatives. For **bis-HYR-7** (Fig. S7), the multivalent version of **HYR-7**, its lowest pKa can be assigned to the protonation of the pyridine group and two higher ones are from the TACN ligand. For **HYR-8**, UV-vis titrations from pH 1.0 to 11.0 reveal changes in the spectra (Fig. S6) that are also best fit with three pKa values: 2.17(6), 4.66(5) and 9.46(2). The lowest pKa value can be assigned to the protonation of the pyridine group on the Aβ binding fragment. In addition, the higher two pKa values are assigned to the amine groups, similar to **HYR-7**. For **bis-HYR-8** (Fig. S8), the multivalent version of **HYR-8**, its lowest pKa can be assigned to the protonation of the pyridine group and two higher ones are from the N4 ligand.

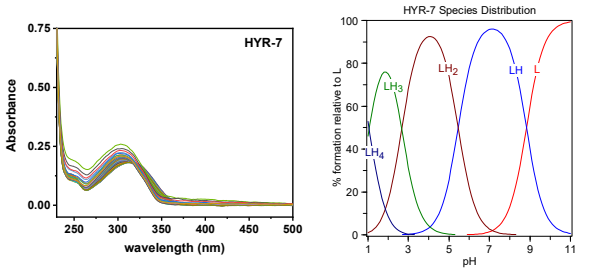

Fig. 2 Variable pH (pH 1-11) titration curve of compound **HYR-7** ([MCC] = 20 μM, 25 °C, I = 0.1 M NaCl) and species distribution plot.

Table 1 Acidity constants (pKa's) of **HYR-7**, **HYR-8**, **bis-HYR-7** and **bis-HYR-8** determined by spectrophotometric titrations (errors are for the last digit)

reaction	HYR-7	HYR-8
$[H_4L]^{3+} = [H_3L]^{2+} + H^+ (pK_{a1})$	1.06(9)	-
$[H_3L]^{2+} = [H_2L]^{+} + H^+ (pK_{a2})$	2.68(7)	2.17(6)
$[H_2L]^{+} = [HL] + H^+ (pK_{a3})$	5.45(3)	4.66(5)
$[HL] = [L]^{-} + H^+ (pK_{a4})$	8.82(2)	9.46(2)
reaction	**bis-HYR-7**	**bis-HYR-8**
$[H_3L]^{2+} = [H_2L]^{+} + H^+ (pK_{a1})$	1.4(3)	1.54(6)
$[H_2L]^{+} = [HL] + H^+ (pK_{a2})$	3.5(2)	5.45(1)
$[HL] = [L]^{-} + H^+ (pK_{a3})$	10.1(1)	8.833(8)

Characterization of Metal complexes

Spectrophotometric titrations were performed to determine the stability constants and solution speciation of Cu^{2+} with MCCs. The pKa values of the ligands were included in the calculations, and the calculated values show that **HYR-7** exhibits larger binding constants (logK's) with Cu^{2+} than **HYR-8**, likely because the TACN ligand is more conformationally flexible than the more rigid N4 ligand and can adopt a favourable geometry for tighter Cu^{2+} binding. Based on the obtained binding constants, solution speciation diagrams were calculated for Cu^{2+} with **HYR-7** and **HYR-8**, showing that the 1:1 Cu:MCC complex is the predominant species formed. In addition, Fig. 3 shows that the concentration of free Cu^{2+} with **HYR-7** is negligible even at very low pH. While adding a second pyridyl-benzothiazole arm to **HYR-7** does not seem to increase the Cu complex stability constant for **bis-HYR-7**, **bis-HYR-8** does show a higher logK for its Cu complex, suggesting that for the N4 ligand the adopted conformation allows for both pyridine N's to potentially interact with the Cu centre.

For a better comparison of the Cu^{2+} binding affinities for these compounds, pCu (−log $[Cu]_{free}$) values were calculated at two pH values (Table 3). Interestingly, the pCu values of the MCCs are higher than the standard strong chelators such as diethylenetriaminepentacetic acid (DTPA).[38] During the titration experiments, the spectral changes observed were immediate, suggesting a fast Cu chelation. This is important for efficient ^{64}Cu radiolabeling, which requires fast complexation. Further stability tests were performed by adding Cu complexes to a solution of 2.5 M HCl (Fig. S13). Even under pH~0 condition, there is no sign of any decomposition in their UV-vis spectra. Overall, these results strongly suggest that all four compounds should be suitable to be used as ^{64}Cu chelating agents.

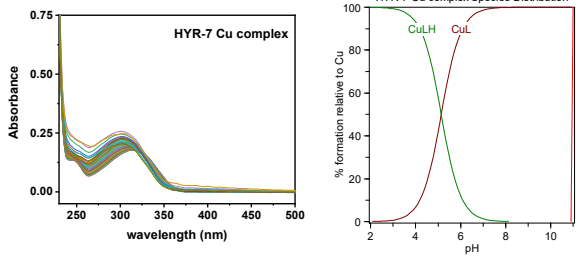

Fig. 3 Variable pH (pH 1-11) UV spectra of **HYR-7** and Cu^{2+} system ([**HYR-7**] = $[Cu^{2+}]$ = 20 µM, 25 °C, I = 0.1 M NaCl) and species distribution plot.

Table 2 Stability constants (log K) of the Cu^{2+} complexes of HYR-7, HYR-8, bis-HYR-7 and bis-HYR-8 (errors are for the last digit)

reaction	HYR-7	HYR-8
$Cu^{2+} + HL = [CuHL]^{2+}$	5.1(7)	9.47(3)
$Cu^{2+} + L^{-} = [CuL]^{+}$	19.4(3)	16.34(1)
reaction	**bis-HYR-7**	**bis-HYR-8**
$Cu^{2+} + HL = [CuHL]^{2+}$	5.0(9)	5.1(7)
$Cu^{2+} + L^{-} = [CuL]^{+}$	19.2(9)	18.7(4)

Table 3 Calculated pCu (−log $[Cu]_{free}$) values for a solution containing a 1:1 metal/ligand mixture ($[Cu^{2+}]_{tot}$ = $[MCC]_{tot}$ = 20 µM)

pH	HYR-7	HYR-8	bis-HYR-7	bis-HYR-8	DTPA
6.6	11.1	10.6	10.3	10.7	9.7
7.4	11.5	10.7	10.8	11.2	10.7

X-ray Structures of Cu Complexes

The **Cu-HYR-7** complex was synthesized, and single crystals were obtained by the slow evaporation of a dichloromethane/ether solution. In **Cu-HYR-7**, the Cu center exhibits a N4Cl square pyramidal coordination environment, with three N atoms from the tacn macrocycle, one pyridine N atom, and one Cl atom (Fig. 4a). The **Cu-HYR-8** complex was also obtained by the slow evaporation of an acetonitrile/ether solution under N_2. In the crystal, the Cu center shows a N5 square pyramidal coordination structure, with four N atoms from the N4 macrocycle, one pyridine N atom (Fig. 4b).

Most importantly, these crystal structures offer solid evidence that the N atom on the pyridine group does interact with the Cu center and thus the structure incorporation strategy is practical for the design of stronger chelating ligands.

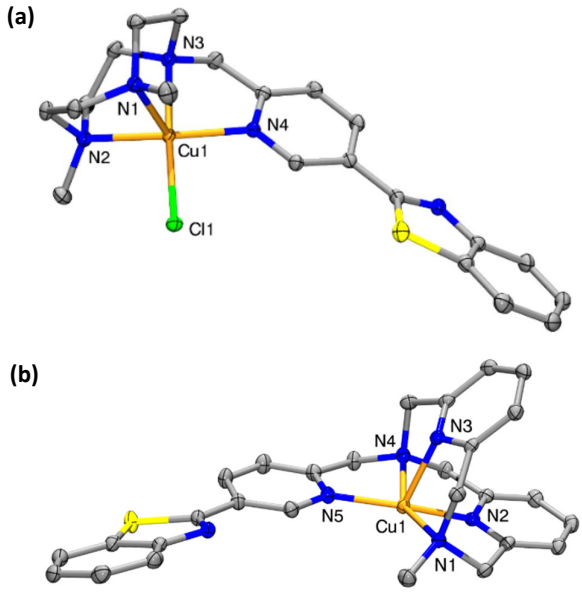

Fig. 4 ORTEP plots of the cations of: (a) **Cu-HYR-7** at the 50% probability level. Perchlorate anions and H atoms are omitted for clarity. Selected bond lengths (Å) Cu1−N1 2.2189(13), Cu1−N2 2.0871(14), Cu1−N3 2.0396(13), Cu1−N4 2.0313(13), Cu1−Cl1 2.2483(4). (b) **Cu-HYR-8** at the 50% probability level. Selected bond lengths (Å) Cu1−N1 2.2881(18), Cu1−N2 1.9347(18), Cu1−N3 2.1706(18), Cu1−N4 2.1146(19), Cu1−N5 1.9773(18).

EPR Spectra of Copper Complexes

To further characterize the Cu-MCC complexes, their X-band EPR spectra were recorded in frozen glasses at 77 K. The EPR spectrum of the **Cu-HYR-7** mononuclear complex in a 1:3 (v/v) MeCN/PrCN frozen solution reveals a pseudoaxial EPR pattern with three different *g* values: g_x = 2.059, g_y = 2.050, and g_z = 2.220 (Fig. 5). Similarly, the EPR spectrum of the **Cu-HYR-8** mononuclear complex in 1:3 (v/v) MeCN/PrCN reveals a pseudoaxial EPR pattern with two different *g* values: g_x = g_y = 2.090, and g_z = 2.270 (Fig. S14). For **Cu-bis-HYR-7**, its EPR spectrum exhibits a pseudoaxial EPR pattern with three different *g* values: g_x = 2.059, g_y = 2.058, and g_z = 2.236 (Fig. S15), suggesting that the complex remains mononuclear in solution, while the EPR spectrum of **Cu-bis-HYR-8** cannot be simulated well, likely due to presence of two different conformations for this Cu complex (Fig. S16).

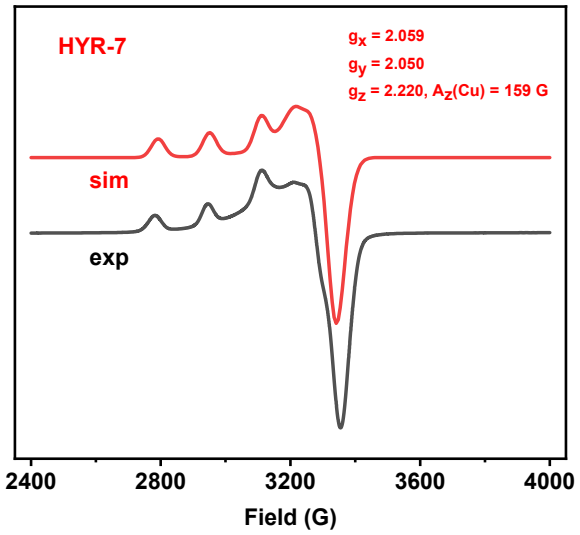

Fig. 5 EPR spectra of the **Cu-HYR-7** mononuclear complex in 1:3 1 M MeCN/PrCN at 77 K. The following parameters were used for the simulations: g_x = 2.059, g_y = 2.050, g_z = 2.220, A_z(Cu) = 159 G.

5xFAD Mouse Brain Section Staining of Metal Complexes

After showing that all metal-binding compounds have appreciable Cu^{2+} affinity, fluorescence imaging studies of 5xFAD mouse brain sections were performed to evaluate the Aβ binding ability of the MCCs. Brain sections from 11-month old 5xFAD mice were treated with **HYR-7**, **HYR-8**, **bis-HYR-7**, and **bis-HYR-8**, respectively (Fig. S17). Interestingly, results reveal significant fluorescent staining of the amyloid plaques, as confirmed by co-staining with the CF594-conjugated HJ3.4 antibody (CF594-HJ3.4) that binds to a wide range of Aβ species.[2-4, 11, 39, 40] Then, fluorescence staining using the corresponding Cu complexes was also performed, since the actual PET imaging agents would be the radiolabeled ^{64}Cu complexes. All Cu(II) complexes stained well the Aβ plaques, as confirmed by CF594-HJ3.4 antibody immunostaining, suggesting that the Cu(II) complexes could be used for the detection of Aβ species (Fig. 6).

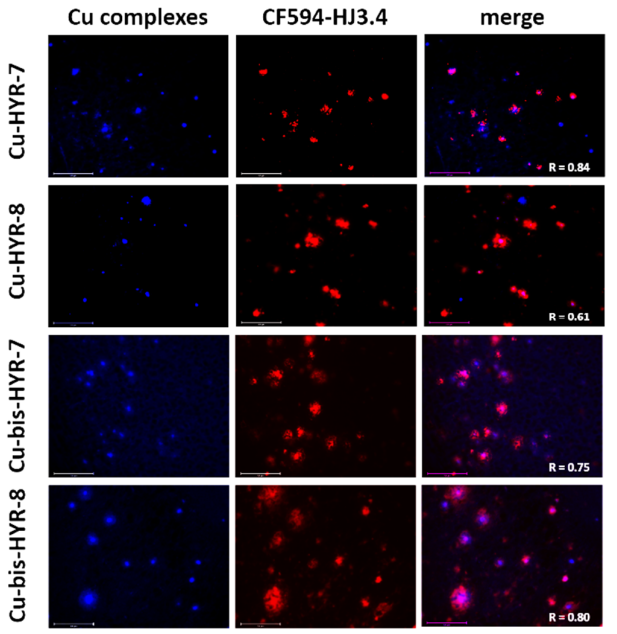

Fig. 6 Fluorescence microscopy images of 5xFAD mice brain sections incubated with metal-chelating Cu complexes. The fluorescence signals from compounds and CF594-HJ3.4 antibody were monitored under blue and red channels, respectively. Scale bar: 125 µm. R is the Pearson's correlation coefficient.

Autoradiography Studies of ^{64}Cu-complexes

Ex vivo autoradiography studies using brain sections of transgenic 5xFAD and age-matched WT mice were also performed to determine the specific binding to the amyloid plaques for the **^{64}Cu-HYR-7**, **^{64}Cu-HYR-8**, **^{64}Cu-bis-HYR-7** and **^{64}Cu-bis-HYR-8** complexes. There is a great contrast between the intensity of WT (Fig. 7a, first row) and 5xFAD (Fig. 7a, third row) for all radiolabeled complexes, especially for **^{64}Cu-HYR-7** with a quantified value of 6.3 (Fig. 7b). Moreover, the specific binding of the ^{64}Cu-labeled complexes to amyloid plaques was confirmed by blocking with the nonradioactive blocking agent **B1** (Fig. S18), which led to a markedly decreased autoradiography intensity (Fig. 6a, second row). In addition, one crucial factor for PET imaging agents of AD is that they need to efficiently cross the blood-brain barrier (BBB). Log D values between 0.9 and 2.5 have been reported to be optimal for promising BBB permeability.[41] The **^{64}Cu-HYR-7** and **^{64}Cu-HYR-8** complexes show relatively low log D values because of their dicationic nature. However, with the introduction of the second hydrophobic fragment, the **^{64}Cu-bis-HYR-7** and **^{64}Cu-bis-HYR-8** complexes exhibit higher log D values, suggesting that they have

the potential to cross the BBB (Fig. 7c). As a result, the latter two complexes were selected to be used in the *in vivo* biodistribution studies.

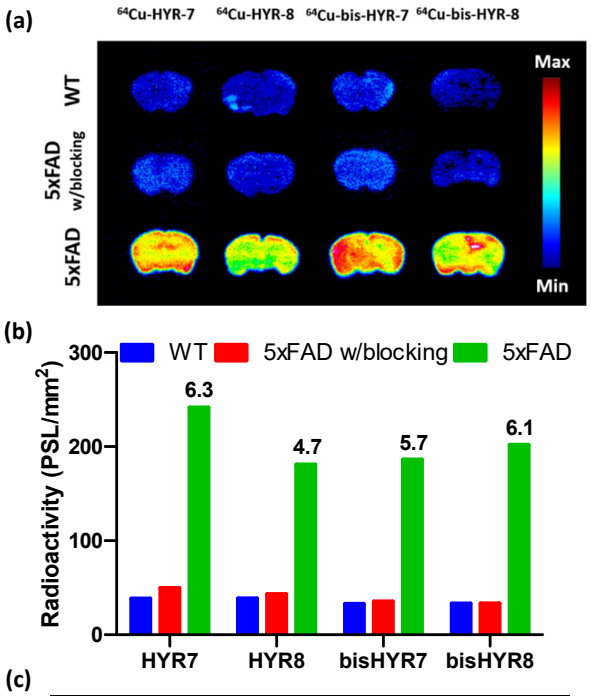

(c)

^{64}Cu complexes	MW (g·mol^{-1})	*log* D_{oct}
^{64}Cu-HYR-7	446.4	0.32 ± 0.02
^{64}Cu-HYR-8	542.5	0.35 ± 0.01
^{64}Cu-bis-HYR-7	655.7	0.99 ± 0.02
^{64}Cu-bis-HYR-8	752.8	0.98 ± 0.03

Fig. 7 (a) Autoradiography images of the brain sections from WT and 5xFAD mice after treatment of **^{64}Cu complexes**, in the absence or presence of a blocking agent. (b) Average intensities of the brain sections in the autoradiography images. The numbers in the bar graph are the intensity ratios of 5xFAD to WT in each group. (c) Partition coefficient (*log* D_{oct}) of corresponding ^{64}Cu complexes in octanol/PBS (pH 7.4).

Biodistribution Studies

After the collection of promising *in vitro* results, *in vivo* biodistribution experiments were performed to investigate the pharmacokinetics of ^{64}Cu-radiolabeled complexes using normal CD-1 mice. The retention and accumulation of the ^{64}Cu-radiolabeled complexes in selected organs were evaluated at 2, 60, and 240 min post-injection. Interestingly, **^{64}Cu-bis-HYR-7** showed higher brain uptake at 2 min with an appreciable accumulation of the radioactivity of ~0.4 %ID/g even after 4 h (Fig. 8c, 8e). However, **^{64}Cu-bis-HYR-8** showed lower brain uptake at 2 min of ~0.2 %ID/g and increased accumulation in brain even after 4 h of ~0.4 %ID/g (Fig. 8d, 8f), indicating that the latter complex takes a longer time to reach the brain. Also, this difference could be due to the higher stability constant of the Cu-bis-HYR-7 complex than that of Cu-bis-HYR-8, suggesting that the N4 ligand in **HYR-8** is too bulky for tighter Cu binding.

Taken together, these studies strongly suggest that **^{64}Cu-bis-HYR-7** system with specific Aβ binding ability is promising for Aβ detection *in vivo*, but further structure modification is necessary to increase its BBB permeability for further application.

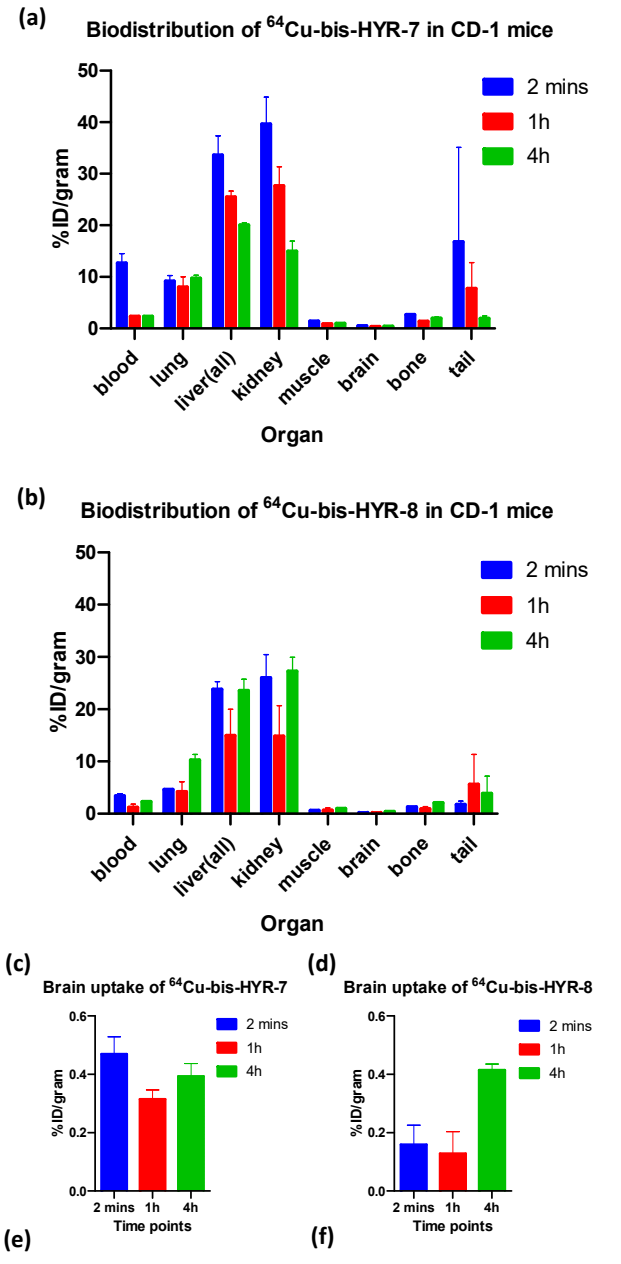

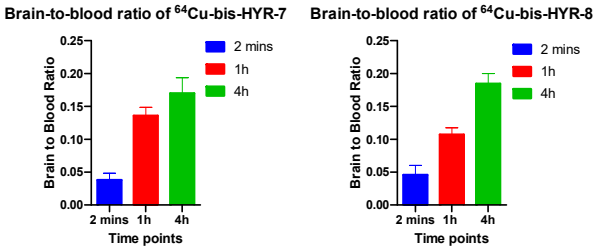

Fig. 8 Biodistribution studies of a) **^{64}Cu-bis-HYR-7** and b) **^{64}Cu-bis-HYR-8** In the organs of CD-1 mice at 2, 60, and 240 min post-injection (% injected dose per gram, %ID per g). Brain uptake for c) **^{64}Cu-bis-HYR-7** and d) **^{64}Cu-bis-HYR-8**. Calculated brain-to-blood ratios from the biodistribution studies for e) **^{64}Cu-bis-HYR-7** and f) **^{64}Cu-bis-HYR-8**.

Conclusions

In conclusion, a series 1,4,7-triazacyclononane (TACN) and 2,11-diaza[3.3]-(2,6)pyridinophane (N4)-based metal-binding compounds with pyridine arms were designed and synthesized by incorporating Aβ interacting fragments into metal-binding chelating ligands. The incorporation strategy increases the metal-binding affinity of the Aβ-interacting fragment, without the loss of Aβ specificity. Although the Log D values and BBB permeability of the investigated Cu complexes are less than optimal, this strategy could lead to improved Cu-chelating and Aβ-binding compounds for ^{64}Cu PET imaging in AD. One solution could be the introduction of carboxylate arms onto the N atoms of the TACN ligand. The resulting hexadentate ligand shaould form 6-coordinate, neutral Cu^{2+} complexes, which are expected to be more hydrophobic and thus exhibit increased BBB permeability.[42]

Overall, the employed approach based on the incorporation strategy can be applied to other ^{64}Cu-based diagnostic PET imaging applications in neurodegenerative diseases.

Author information

Corresponding author

mirica@illinois.edu; b.rogers@wustl.edu

ORCID

Liviu M. Mirica: 000-0003-0584-9508
Yiran Huang: 0000-0003-1755-9874
Liang Sun: 0000-0002-0080-0855

Conflicts of interest

There are no conflicts to declare.

Acknowledgements

L.M.M. acknowledges research funding from the NIH (R01GM114588). The authors would like to thank the small animal imaging facility at Washington University School of Medicine for excellent technical assistance, Cedric Mpoy for valuable assistance with animal studies, the Isotope Production Group at Washington University for production of ^{64}Cu, and Toby Woods for the help with solving the crystal structures.

References

1. *Alzheimer's & Dementia*, 2020, **16**, 391-460.
2. M. Ono and H. Saji, *MedChemComm*, 2015, **6**, 391-402.
3. A. G. Vlassenko, T. L. S. Benzinger and J. C. Morris, *Biochim. Biophys. Acta, Mol. Basis Dis.*, 2012, **1822**, 370-379.
4. D. J. Hayne, S. Lim and P. S. Donnelly, *Chem. Soc. Rev.*, 2014, **43**, 6701-6715.
5. V. L. Villemagne, V. Doré, S. C. Burnham, C. L. Masters and C. C. Rowe, *Nat. Rev. Neurol.*, 2018, **14**, 225-236.
6. S. R. Choi, J. A. Schneider, D. A. Bennett, T. G. Beach, B. J. Bedell, S. P. Zehntner, M. J. Krautkramer, H. F. Kung, D. M. Skovronsky, F. Hefti and C. M. Clark, *Alz. Dis. Assoc. Dis.*, 2012, **26**, 8-16.
7. D. A. Wolk, Z. Zhang, S. Boudhar, C. M. Clark, M. J. Pontecorvo and S. E. Arnold, *J Neurol Neurosur Ps*, 2012, **83**, 923-926.
8. C. Carswell, K. Muckle, A. Waldman, Z. Win, P. Malhotra and R. Perry, *J Neurol Neurosur Ps*, 2016, **87**.
9. M. Boccardi, D. Altomare, C. Ferrari, C. Festari, U. P. Guerra, B. Paghera, C. Pizzocaro, G. Lussignoli, C. Geroldi, O. Zanetti, M. S. Cotelli, M. Turla, B. Borroni, L. Rozzini, D. Mirabile, C. Defanti, M. Gennuso, A. Prelle, S. Gentile, A. Morandi, S. Vollaro, G. Dalla Volta, A. Bianchetti, M. Z. Conti, M. Cappuccio, P. Carbone, D. Bellandi, L. Abruzzi, L. Bettoni, D. Villani, M. C. Raimondi, A. Lanari, A. Ciccone, E. Facchi, I. Di Fazio, R. Rozzini, S. Boffelli, L. Manzoni, G. P. Salvi, S. Cavaliere, G. Belotti, S. Avanzi, P. Pasqualetti, C. Muscio, A. Padovani, G. B. Frisoni and I. D. Value, *JAMA Neurol.*, 2016, **73**, 1417-1424.
10. S. R. Khan, N. H. Patel, K. L. Wallitt, N. D. Soneji, D. Fakhry-Darian, C. J. Carswell, P. A. Malhotra, R. Perry, K. S. Nijran, S. Khan, W. Svensson, T. D. Barwick and Z. Win, *Eur. J. Nucl. Med. Mol. Imaging*, 2016, **43**, S624-S624.
11. A. C. Sedgwick, J. T. Brewster, P. Harvey, D. A. Iovan, G. Smith, X.-P. He, H. Tian, J. L. Sessler and T. D. James, *Chem. Soc. Rev.*, 2020, **49**, 2886-2915.
12. J. L. Hickey, S. Lim, D. J. Hayne, B. M. Paterson, J. M. White, V. L. Villemagne, P. Roselt, D. Binns, C. Cullinane, C. M. Jeffery, R. I. Price, K. J. Barnham and P. S. Donnelly, *J. Am. Chem. Soc.*, 2013, **135**, 16120-16132.
13. J. L. Hickey and P. S. Donnelly, *Coord. Chem. Rev.*, 2012, **256**, 2367-2380.
14. J. L. Hickey, S. Lim, D. J. Hayne, B. M. Paterson, J. M. White, V. L. Villemagne, P. Roselt, D. Binns, C. Cullinane, C. M. Jeffery, R. I. Price, K. J. Barnham and P. S. Donnelly, *J. Am. Chem. Soc.*, 2013, **135**, 16120-16132.
15. L. E. McInnes, A. Noor, K. Kysenius, C. Cullinane, P. Roselt, C. A. McLean, F. C. K. Chiu, A. K. Powell, P. J. Crouch, J. M. White and P. S. Donnelly, *Inorg. Chem.*, 2019, **58**, 3382-3395.
16. M. T. Fodero-Tavoletti, V. L. Villemagne, B. M. Paterson, A. R. White, Q. X. Li, J. Camakaris, G. J. O'Keefe, R. Cappai, K. J. Barnham and P. S. Donnelly, *J. Alzheimers Dis.*, 2010, **20**, 49-55.
17. A. J. Chang, R. Sohn, Z. H. Lu, J. M. Arbeit and S. E. Lapi, *PLoS One*, 2013, **8**, 1-8.
18. X. Nie, R. Laforest, A. Elvington, G. J. Randolph, J. Zheng, T. Voller, D. R. Abendschein, S. E. Lapi and P. K. Woodard, *J. Nucl. Med.*, 2016, **57**, 2006-2011.

19. A. K. Sharma, J. W. Schultz, J. T. Prior, N. P. Rath and L. M. Mirica, *Inorg. Chem.*, 2017, **56**, 13801-13814.
20. K. Chen and M. Cui, *MedChemComm*, 2017, **8**, 1393-1407.
21. A. K. Sharma, S. T. Pavlova, J. Kim, D. Finkelstein, N. J. Hawco, N. P. Rath, J. Kim and L. M. Mirica, *J. Am. Chem. Soc.*, 2012, **134**, 6625-6636.
22. A. K. Sharma, S. T. Pavlova, J. Kim, J. Kim and L. M. Mirica, *Metallomics*, 2013, **5**, 1529-1536.
23. A. K. Sharma, J. Kim, J. T. Prior, N. J. Hawco, N. P. Rath, J. Kim and L. M. Mirica, *Inorg. Chem.*, 2014, **53**, 11367-11376.
24. N. Bandara, A. K. Sharma, S. Krieger, J. W. Schultz, B. H. Han, B. E. Rogers and L. M. Mirica, *J. Am. Chem. Soc.*, 2017, **139**, 12550-12558.
25. Y. R. Huang, H. J. Cho, N. Bandara, L. Sun, D. Tran, B. E. Rogers and L. M. Mirica, *Chem. Sci.*, 2020, **11**, 7789-7799.
26. S. El Ghachtouli, C. Cadiou, I. Dechamps-Olivier, F. Chuburu, M. Aplincourt and T. Roisnel, *Eur. J. Inorg. Chem.*, 2006, , 3472-3481.
27. R. Delgado, V. Felix, L. M. P. Lima and D. W. Price, *Dalton Trans.*, 2007, **36**, 2734-2745.
28. T. Storr, K. H. Thompson and C. Orvig, *Chem. Soc. Rev.*, 2006, **35**, 534-544.
29. L. M. P. Lima, D. Esteban-Gómez, R. Delgado, C. Platas-Iglesias and R. Tripier, *Inorg. Chem.*, 2012, **51**, 6916-6927.
30. M. G. Savelieff, G. Nam, J. Kang, H. J. Lee, M. Lee and M. H. Lim, *Chem. Rev.*, 2019, **119**, 1221-1322.
31. C. Zhang, L. M. F. Gomes, T. Zhang and T. Storr, *Can. J. Chem.*, 2017, **96**, 78-82.
32. C. Dyrager, R. P. Vieira, S. Nyström, K. P. R. Nilsson and T. Storr, *New J. Chem.*, 2017, **41**, 1566-1573.
33. M. Roger, L. M. P. Lima, M. Frindel, C. Platas-Iglesias, J.-F. Gestin, R. Delgado, V. Patinec and R. Tripier, *Inorg. Chem.*, 2013, **52**, 5246-5259.
34. A. Guillou, L. M. P. Lima, M. Roger, D. Esteban-Gomez, R. Delgado, C. Platas-Iglesias, V. Patinec and R. Tripier, *Eur J Inorg Chem*, 2017, 2435-2443.
35. C. Bazzicalupi, A. Bencini, E. Faggi, A. Garau, C. Giorgi, V. Lippolis, A. Perra and B. Valtancoli, *Dalton Trans*, 2006, **35**, 1409-1418.
36. M. Mameli, M. C. Aragoni, M. Arca, M. Atzori, A. Bencini, C. Bazzicalupi, A. J. Blake, C. Caltagirone, F. A. Devillanova, A. Garau, M. B. Hursthouse, F. Isaia, V. Lippolis and B. Valtancoli, *Inorg Chem*, 2009, **48**, 9236-9249.
37. M. Le Fur, M. Beyler, N. Le Poul, L. M. P. Lima, Y. Le Mest, R. Delgado, C. Platas-Iglesias, V. Patinec and R. Tripier, *Dalton Trans.*, 2016, **45**, 7406-7420.
38. A. E. Martell and R. M. Smith, *Critical Stability Constants*, Plenum, New York, 1976.
39. R. J. Perrin, A. M. Fagan and D. M. Holtzman, *Nature*, 2009, **461**, 916-922.
40. A. Nordberg, *Lancet Neurol.*, 2004, **3**, 519-527.
41. D. D. Dischino, M. J. Welch, M. R. Kilbourn and M. E. Raichle, *J. Nucl. Med.*, 1983, **24**, 1030-1038.
42. H. J. Cho, T. T. Huynh, B. E. Rogers and L. M. Mirica, *Proc Natl Acad Sci U S A*, 2020, **117**, 30928-30933.

TOC Graphic